ELSEVIER

NeuroImage

www.elsevier.com/locate/ynimg
NeuroImage 25 (2005) 1077–1089

Hippocampal shape analysis using medial surfaces

Sylvain Bouix,[a,b,*] Jens C. Pruessner,[c] D. Louis Collins,[c] and Kaleem Siddiqi[d]

[a]*Department of Psychiatry, Boston VA Healthcare System, Harvard Medical School, Boston, MA 02115, USA*
[b]*Surgical Planning Laboratory, Brigham and Women's Hospital, Harvard Medical School, Boston, MA 02115, USA*
[c]*McConnell Brain Imaging Centre, McGill University, Montréal, QC, Canada*
[d]*School of Computer Science, McGill University, Montréal, QC, Canada*

Received 9 July 2004; revised 2 December 2004; accepted 16 December 2004
Available online 25 February 2005

In magnetic resonance imaging (MRI) research, significant attention has been paid to the analysis of the hippocampus (HC) within the medial temporal lobe because of its importance in memory and learning, and its role in neurodegenerative diseases. Manual segmentation protocols have established a volume decline in the HC in conjunction with Alzheimer's disease, epilepsy, post-traumatic stress disorder, and depression. Furthermore, recent studies have investigated age-related changes of HC volume which show an interaction with gender; in early adulthood, volume reduction of the HC is found in men but not in women. In this paper, we investigated gender differences in normal subjects in young adulthood by employing a shape analysis of the HC using medial surfaces. For each subject, the most prominent medial manifold of the HC was extracted and flattened. The flattened sheets were then registered using both a rigid and a non-rigid alignment technique, and the medial surface radius was expressed as a height function over them. This allowed for an investigation of the association between subject variables and the local width of the HC. With regard to the effects of age and gender, it could be shown that the previously observed gender differences were mostly due to volume loss in males in the lateral areas of the HC head and tail. We suggest that the analysis of HC shape using medial surfaces might thus serve as a complimentary technique to investigate group differences to the established segmentation protocols for volume quantification in MRI.

Keywords: MRI; Structural analysis; Medial temporal lobe; Medial surfaces; Hippocampus; Shape analysis

Introduction

Magnetic resonance imaging (MRI) is a frequently used tool by neuroscientists and clinicians for volumetric analysis of specific structures of the central nervous system (CNS). In neurodegenerative diseases like Alzheimer's, a region that has been especially prone to volume loss is the medial temporal lobe (MTL), and the specific structures contained within the MTL, like the hippocampus (HC) and parahippocampal gyrus (PHG). These structures are also implicated in post-traumatic stress disorder, epilepsy, depression, and normal aging. Finally, the structures of the MTL are frequently investigated for their involvement in acquisition and retention of memory (Corkin et al., 1997; Mori et al., 1997; Schacter and Wagner, 1999), clearly indicating a need for precise analysis of their involvement in these conditions and functions. In MRI, investigation of these structures is often done using manual segmentation protocols, which yield a quantification of the space the structure occupies within the CNS. Although this technique can successfully demonstrate the involvement of the HC and the PHG in neurodegenerative disease, specific disorders, memory function, and normal aging, it is incapable of showing changes within the structure, taking only the total volume into account. Alternative techniques like voxel-based morphometry (VBM) are not based on manual segmentation of specific structures and do not allow significant findings to be interpreted as evidence of volume loss. Taken together, a precise definition of volume loss within structures in conjunction with normal aging, memory functions, or specific disease states is missing, justifying the need for the development of additional analysis tools.

In both clinical and research contexts, quantitative models for the three-dimensional (3D) shape of these structures might allow an alternative approach for the statistical analysis of their distinct characteristics. In fact, there has been significant progress in the development of such methods for use in computational anatomy, as described by several recent articles in Thomson et al. (2004). A first class of methods uses a feature vector, e.g., determined by spherical harmonics or invariant moment representations (Brechbuhler et al., 1995; Mangin et al., 2003), and attempts to

* Corresponding author. Surgical Planning Laboratory, Brigham and Women's Hospital, Harvard Medical School, Boston, MA 02115, USA.
E-mail addresses: sylvain@bwh.harvard.edu (S. Bouix), jens@bic.mni.mcgill.ca (J.C. Pruessner), louis@bic.mni.mcgill.ca (D. Louis Collins), siddiqi@cim.mcgill.ca (K. Siddiqi).
Available online on ScienceDirect (www.sciencedirect.com).

1053-8119/$ - see front matter © 2004 Elsevier Inc. All rights reserved.
doi:10.1016/j.neuroimage.2004.12.051

discriminate between classes of shapes using clustering techniques. Such methods are usually numerically stable and allow for the computation of relevant statistics. However, the representations are coarse and hence an interpretation of the results in terms of anatomical changes can be difficult. A second class of methods is based on a representation of an object's surface or interior, along with a study of the mechanical deformations required to transform one object into another (Bookstein, 1997; Cootes et al., 1995; Csernansky et al., 1998). This popular technique is very intuitive, but relies on the use of registration techniques which can be difficult to implement. The calculation of significant statistics from the recovered deformation fields also poses a challenge. A third class makes use of medial representations which provide information on an object's reflective symmetries. Unfortunately, these medial models still need to be registered with each other before any statistics can be derived (Bouix et al., 2001; Styner et al., 2003a). In clinical studies, different classes of methods are often combined in order to obtain intuitive and statistically significant results, see for example Styner et al. (2003b). With respect to structures such as the HC, this last class of methods is attractive because it can be shown that the number of medial surface manifolds is small and hence the representation is compact. The most prominent sheet can be used to register individual data sets in an object-centered way, followed by more precise comparisons (Styner and Gerig, 2001).

Medial models have been successfully used in medical image analysis in a number of contexts, see Golland et al. (1999) and Pizer et al. (1999) for some recent applications. Applying these methods in 3D presents an additional challenge because only a small class of computationally reliable algorithms exist. One such class relies on pruning strategies for 3D Voronoi diagrams (Attali et al., 1997; Näf et al., 1996). Styner and Gerig (2001) have recently developed such a framework where medial models developed by Pizer et al. (2003) and Joshi et al. (2001) are used to segment the HC and spherical harmonics along with a coarse-scale sampled medial description are used to represent its shape.

In this paper, we adopt a similar strategy, but use a novel algorithm we have developed for computing medial surfaces. We apply this method to the analysis of a HC data set for which a volume loss with age in young adulthood has been previously observed in normal male subjects but not in normal females (Pruessner et al., 2001). Our hypothesis is that the volume loss is not uniform over the HC, but is rather localized to specific regions. Our goal is to locate these regions of volume loss as well as the regions where gender differences are most prominent, and to quantify the strength of these effects. To do so, we extract the most prominent medial sheet of the HC for each subject and then flatten it. We then register the flattened sheets in a common coordinate frame using both a rigid and a non-rigid alignment technique. This allows us to express the medial surface radius, which indicates the local width of the HC, as a height function over each flattened surface. We then carry out a statistical examination of the relationship between gender and age and local object width. Our main finding is that the previously observed gender differences were mostly due to volume loss in males in the lateral areas of the HC head and tail.

Materials and methods

Hippocampal data

In a previously published analysis (Pruessner et al., 2001), the left and right HC and AG were manually segmented from T1-weighted MR images (three-dimensional spoiled gradient echo acquisition with sagittal volume excitation; repetition time 18 ms, echo time 10 ms, flip angle 30°: 1 mm^3 voxels) from 80 normal healthy subjects. These subjects included 39 healthy men and 41 healthy women in the age range of 18–42 years (mean age 25.09 ± 4.9 years). The MRI data for each subject were first corrected for image intensity non-uniformity (Sled et al., 1998) and linearly registered to a standard brain-based coordinate system known as stereotaxic space (Collins et al., 1994). It was then segmented manually by 3D voxel painting using a recently developed segmentation protocol for the HC in normal controls in early adulthood (Pruessner et al., 2000). By resampling with a tri-cubic interpolation kernel onto a 1 mm^3 voxel grid in stereotaxic space (Collins et al., 1994), each brain volume was normalized for size, orientation, and position. A typical segmentation of an individual HC is shown in Fig. 1.

A quantitative analysis of the original label volumes derived from the MR images revealed an overall hemispheric difference with the right HC being bigger than the left (4300 vs. 4072 mm^3, $P < 0.001$). Furthermore, there was a correlation with age in the group of men for both the left and the right HC (Spearman's $r = -0.44$, $P < 0.005$) that was not apparent in the group of women ($r = 0.01$, $P > 0.20$). In order to determine the location of these differences, a regression analysis was applied to each voxel with image intensity as the dependent variable (Pruessner et al., 2001). Since nearby voxels were expected to be correlated, the technique of Worsley et al. (1998) was used to determine the critical threshold to identify statistically significant regressions. The analysis revealed that differences between men and women seemed to occur mostly in the head and tail of the HC. However, it was not possible to determine whether the observed differences were due only to a volume reduction or

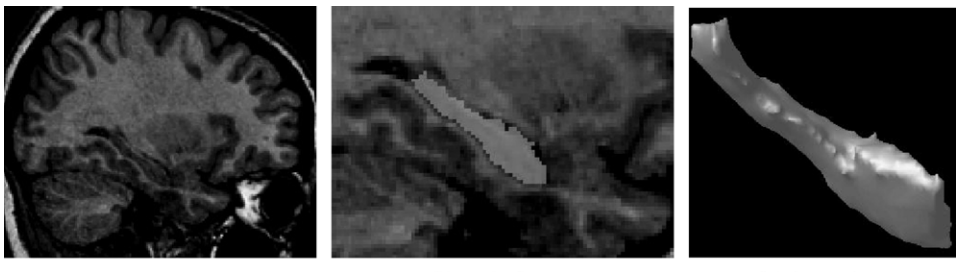

Fig. 1. Hippocampal data from one subject. (a) A sagittal T1-weighted MR image. (b) A zoomed sub-image centered on the HC, which is manually segmented (labeled). (c) An enlarged 3D view of the labeled HC.

were associated with the overall shape of the HC as well. The medial surface algorithm presented here extends the possibilities for analysis, allowing for the investigation of shape differences in the HC between men and women. We chose to focus this analysis on the radius function of the medial surface of the HC, which indicates the local width of this structure at different locations in the medial temporal lobe.

Average outward flux based medial surfaces

This section presents an overview of the skeletonization algorithm introduced in Siddiqi et al. (2002). Beginning with a binary volume as its input, this algorithm produces a digitized version of the 3D skeleton or medial axis (Blum, 1973). Formally, the 3D skeleton is the locus of centers of all maximal inscribed spheres within the volume, along with their radius values. In what follows we shall refer to the 3D skeleton as the medial surface, since almost all points of this structure lie on two-dimensional (2D) manifolds in 3D. A formal classification of the types of points on the 3D skeleton is presented in Giblin and Kimia (2004).

The medial surface provides a compact description of a volumetric object while reflecting its local symmetries, as illustrated in Fig. 2. A portion of a medial surface is shown in pink, the surface patches to which it corresponds are shown in blue and the maximal inscribed sphere in black. Intuitively, each point Q on the medial manifold is associated with two distinct points P_1, P_2 on the object's surface to which it is closest in the sense of Euclidean distance. The points P_1 and P_2 are often referred to as the bi-tangent points of Q, since at each such point the maximal inscribed sphere and the surface of the object share a tangent plane. On a single medial manifold, this mapping of medial manifold points to surface points is one-to-two and onto. Hence, the radius function along with the medial surface can be viewed as describing the local width of the object. The object's surface can be reconstructed by considering the envelope of all the spheres drawn at all medial surface points.

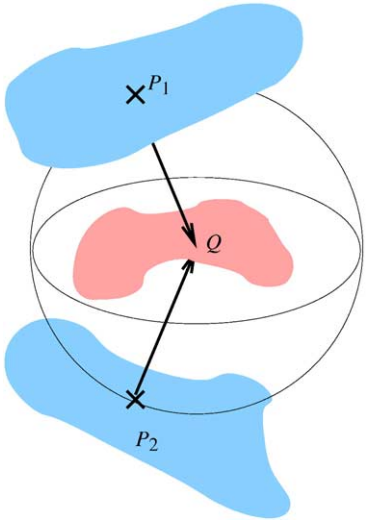

Fig. 2. A portion of a medial surface is shown in pink, the surface patches to which it corresponds are shown in blue and the maximal inscribed sphere in black. Each point Q on the medial manifold is associated with two distinct points P_1, P_2 on the object's surface to which it is closest in the sense of Euclidean distance (see text).

The Hamilton Jacobi formulation

We now review the algorithm on which the subsequent analysis of HC shape is based. For details we refer the reader to Siddiqi et al. (2002). Consider the grassfire flow

$$\frac{\partial \mathcal{S}}{\partial t} = \mathcal{N} \tag{1}$$

acting on a closed 3D surface $\mathcal{S}$, such that each point on its boundary is moving with unit speed in the direction of the inward normal $\mathcal{N}$. In physics, such equations are typically solved by looking at the evolution of the phase space of an equivalent Hamiltonian system. Let D be the Euclidean distance function to the initial surface $\mathcal{S}_0$ (Borgefors, 1984). The magnitude of its gradient, $\|\nabla D\|$, is identical to 1 in its smooth regime. With $\boldsymbol{q} = (x, y, z)$, $\boldsymbol{p} = (D_x, D_y, D_z)$, and $\|\boldsymbol{p}\| = 1$, the Hamiltonian system is given by

$$\boldsymbol{p} = (0,0,0), \quad \boldsymbol{q} = \left(D_x, D_y, D_z\right) \tag{2}$$

with an associated Hamiltonian function $H = 1 + \|\nabla D\|$. The discrimination of medial from non-medial surface points can be approached by computing the "average outward flux" of the vector field $\boldsymbol{q}$ at a point. This quantity is given by

$$\text{Average Outward Flux}(\boldsymbol{q}) = \frac{\int_{\delta R} \langle \boldsymbol{q}, \mathcal{N}_0 \rangle \mathrm{d}\mathcal{S}}{\text{area}(\delta R)} \tag{3}$$

where $\mathrm{d}\mathcal{S}$ is a surface area element of the bounding surface δR of a volume R and $\mathcal{N}_0$ is the outward normal at each point on the surface. It can be shown that as the volume shrinks to a point not on the medial surface, the average outward flux approaches zero. In contrast, when the volume over which it is computed shrinks to a medial surface point, the average outward flux approaches a strictly negative number (Dimitrov et al., 2003; Siddiqi et al., 2002). Thus, it is an effective way for distinguishing between these two cases. This calculation is used to guide a thinning process in a cubic lattice, while taking care to preserve the object's topology.

Preserving topology

A point is a simple point if its removal does not change the topology of the object. Hence in 3D, its removal must not disconnect the object, create a hole, or create a cavity. Malandain et al. (1993) have introduced a topological classification of a point x in a cubic lattice by computing two numbers:

- C^*: the number of 26-connected components 26-adjacent to x in $O \cap N_{26}^*$
- $\bar{C}$: the number of 6-connected components 6-adjacent to x in $\bar{O} \cap N_{18}^*$

where O is the 26-connected object, $\bar{O}$ is its complement (the 6-connected background), N_{26}^* is the 26 neighborhood of x without x, and N_{18} is the 18 neighborhood of x including x. Further, they have shown that if $C^* = 1$ and $\bar{C} = 1$, the point is simple, and hence removable.

Our basic strategy now is to guide the thinning of the object by the average outward flux measure computed over a very small neighborhood. Points with the most negative average outward flux are the strongest medial surface points. The process is stopped when all surviving points are not simple or have an average outward flux below some chosen (negative) value, or

both. Unfortunately, the result is not guaranteed to be a thin set, i.e., one without an interior.

This last constraint can be satisfied by defining an appropriate notion of an endpoint in a cubic lattice. In R^3, if there exists a plane that passes through a point x such that the intersection of the plane with the object includes an open curve which ends at x, then x is an end point of a 3D curve, or is on the rim or corner of a 3D surface. This criterion can be discretized easily to 26-connected digital objects by examining 9 digital planes in the 26-neighborhood of x (Pudney, 1998). The thinning process proceeds as before, but the threshold criterion for removal is applied only to endpoints. A full description of the procedure is given in Algorithm 1.

Algorithm 1: Average Outward Flux Ordered Thinning.
Part I: Average Outward Flux
Compute the Euclidean Distance Transform D of the object;
Compute the gradient vector field ∇ D;
Compute the average outward ux of ∇ D using Eq. 3;
for (*each point x in the interior of the object*) **do**
  Flux(x) $= \frac{1}{n}\sum_{i=1}^{26}\langle \mathcal{N}_i, \nabla D(x_i)\rangle$;
  (where x_i is a 26-neighbor of x and $\mathcal{N}_i$ is the outward normal at x_i of the unit sphere centered at x)
Part II: Topology Preserving Thinning
for (*each point x on the boundary of the object*) **do**
  if (*x is simple*) **then**
    insert (x, Heap) with Flux(x) as the sorting key for insertion;
while (*Heap.size* > 0) **do**
  x = HeapExtractMax(Heap);
  if (*x is simple*) **then**
    if (*x is an end point*) *and* (Flux(x) < *Thresh*) **then**
    mark x as a skeletal (end) point;
    else
  Remove x;
  for (*all neighbors y of x*) **do**
    if (*y is simple*) **then**
    insert(y, Heap);

Labeling the medial surface

Points on the medial surface can now be labeled as border points, curve points, surface points, or junction points using the classification of Malandain et al. (1993). However, certain special configurations of voxels can lead to misclassification of junction points as surface points and these cases have to be dealt with using a definition for simple surfaces (Malandain et al., 1993).

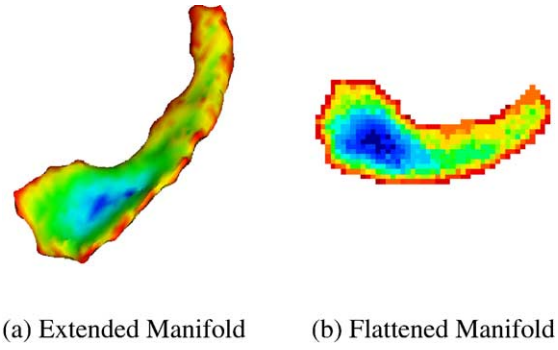

(a) Extended Manifold (b) Flattened Manifold

Fig. 4. A flattening which approximately preserves the distance between any two points leads to an accurate 2D representation (b) of the original extended medial manifold (a). The coloring represents increasing Euclidean distance (from red to blue) of each medial manifold point to the surface of the original object.

Let x be a surface point ($\bar{C} = 2$ and $C^* = 1$). Let A_x and B_x be the two connected components of $\bar{O} \cap N_{18}$ 6-adjacent to x. Two surface points x and y are in an equivalence relation if there exists a 26-path $x_0, x_1, \ldots, x_i, \ldots, x_n$ with $x_0 = x$ and $x_n = y$ such that for $i \in [0, \ldots, n-1]$, ($A_{xi} \cap A_{xi+1} \neq \emptyset$; and $B_{xi} \cap B_{xi+1} \neq \emptyset$) or ($A_{xi} \cap B_{xi+1} \neq \emptyset$; and $B_{xi} \cap A_{xi+1} \neq \emptyset$;). A simple surface is defined as any equivalence class of this equivalence relation.

All the distinct simple surfaces comprising the medial surface can be detected automatically. The essential idea is to use a point on the medial surface as a "source" and to build its corresponding simple surface via a depth first search strategy. This process is carried out recursively and terminates when all medial surface points have been used.

The extended medial manifold

The process of parsing the medial surface of each HC volume (described in Hippocampal data) into its distinct simple surfaces revealed that across the entire population there was a single prominent sheet and only a small number of additional sheets. Furthermore, these additional sheets played essentially no role with regard to shape description: with only one exception, the volume reconstructed by the most prominent sheet was less than 1% different than that reconstructed by the entire medial surface. Thus, in what follows, we focus our analysis on this prominent sheet, which we refer to as the medial manifold.

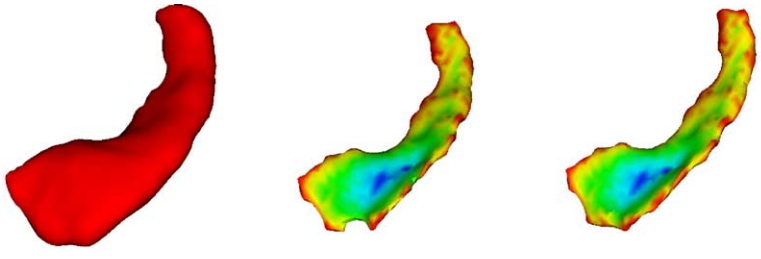

(a) Original Volume (b) Medial Manifold (c) Extended Medial Manifold

Fig. 3. The rim of the medial manifold is extended to the corresponding closest boundary points on the original HC, thus removing some of its variability. The coloring of the original and extended medial manifolds is according to increasing Euclidean distance (from red to blue) from the boundary.

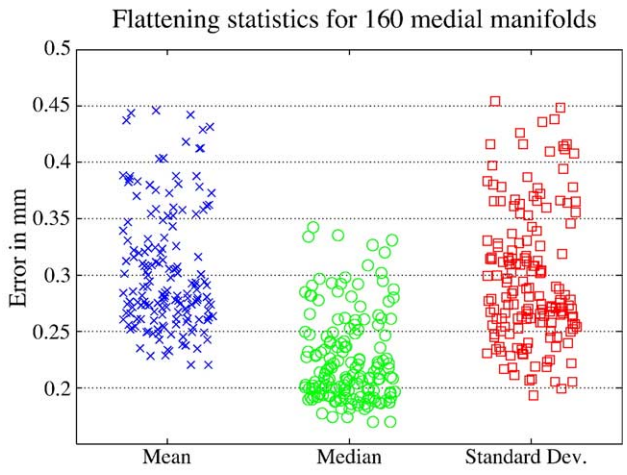

Fig. 5. Statistics of the inter-distance errors introduced by the flattening algorithm for all pairs of points over all 160 medial manifolds.

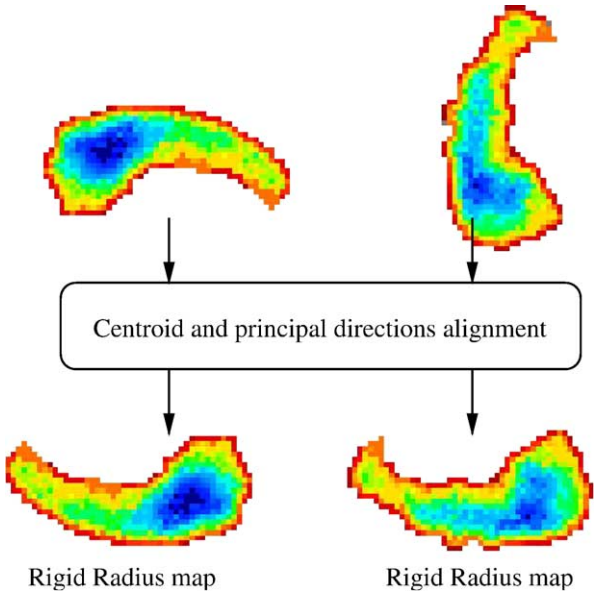

Fig. 7. A rigid alignment between the flattened medial manifolds is computed using the centroids and principal axes of each to define a common coordinate frame.

The key issue now is to establish a method by which to align the medial manifolds derived from each individual subject's HC data so that a statistical analysis of shape can be carried out. In general, the problem of finding a correspondence between two manifolds is an area of ongoing research in the image analysis and computer vision communities, and the precise choice of technique is usually domain and application dependent. With regard to the HC medial manifolds, an issue that arises is that there is considerable variation in the shape of the outer rim (the bounding contour). Intuitively, the medial manifold shrinks in area locally as the corresponding HC cross-section becomes circular (the neck-like regions in Fig. 3b). It is advantageous to reduce this variability and ensure a larger overlap between the sheets to better drive the ensuing alignment process.

We proceed to do this by smoothly extending the rim of each medial manifold to the boundary of the original HC by following the direction of the gradient ∇D of the Euclidean distance function D (see The Hamilton Jacobi formulation). With the exception of very specific degenerate configurations, each point on the rim has a unique corresponding closest point in the sense of Euclidean distance to the boundary of the object (Damon, 2003; Giblin and Kimia, 2004), and thus this extension is mathematically sound. The outcome of this process is illustrated in Fig. 3, where the coloring of the medial manifold points is according to increasing Euclidean distance (from red to blue) from the boundary.

Establishing correspondences between extended medial manifolds

Motivation

One approach to establishing correspondences between the extended medial manifolds so that shape variation across a population can be studied is to associate each sheet with a common coordinate frame by fitting a coarsely sampled medial model to it, as in Styner and Gerig (2001). Whereas this leads to a one-to-one correspondence between the sheets, the deformation each medial manifold has to undergo to fit the common frame can itself introduce shape changes. Such changes can be quite significant particularly when there is variation in medial manifold shape, as is expected across the HC data set. This will in turn have

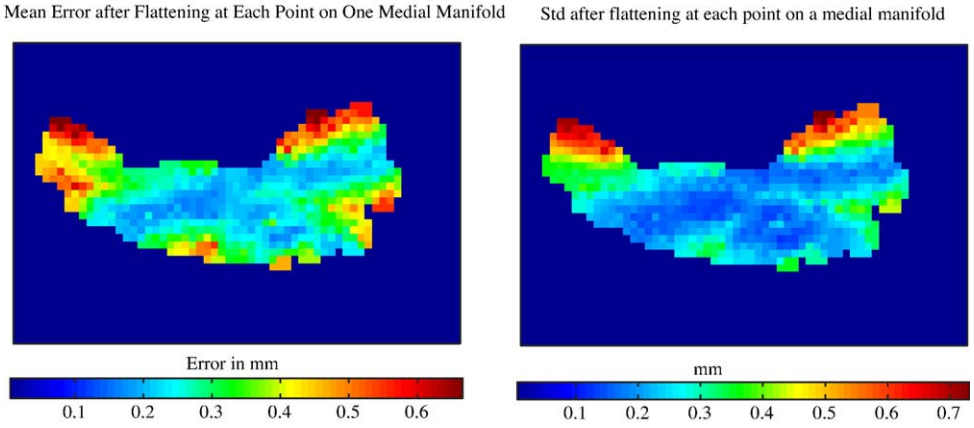

Fig. 6. Mean (left) and standard deviation (right) of the inter-distance errors caused by flattening of a single medial manifold. At each point the mean and standard deviation are computed by considering pairwise distance errors to all other points on the medial manifold.

an impact on the subsequent statistical analysis, which will not only reflect shape changes that are due to anatomical differences but also variations that are introduced by the fitting process.

In our framework, we first employ a flattening of each medial manifold onto a 2D plane which approximately preserves the distance between any two points on it. This allows local properties of the manifold, such as the radius, to be viewed as height functions above the plane (mappings of the form $R^2 \rightarrow R$). We then consider methods for registering the flattened manifolds. First, the manifolds are aligned taking their centroid as the origin and using the principal axes of variation as the coordinate directions. This, being a rigid body transform, introduces no deformation to the flattened manifolds, but does not guarantee a one-to-one correspondence between all points. Second, we employ the *Demons* registration

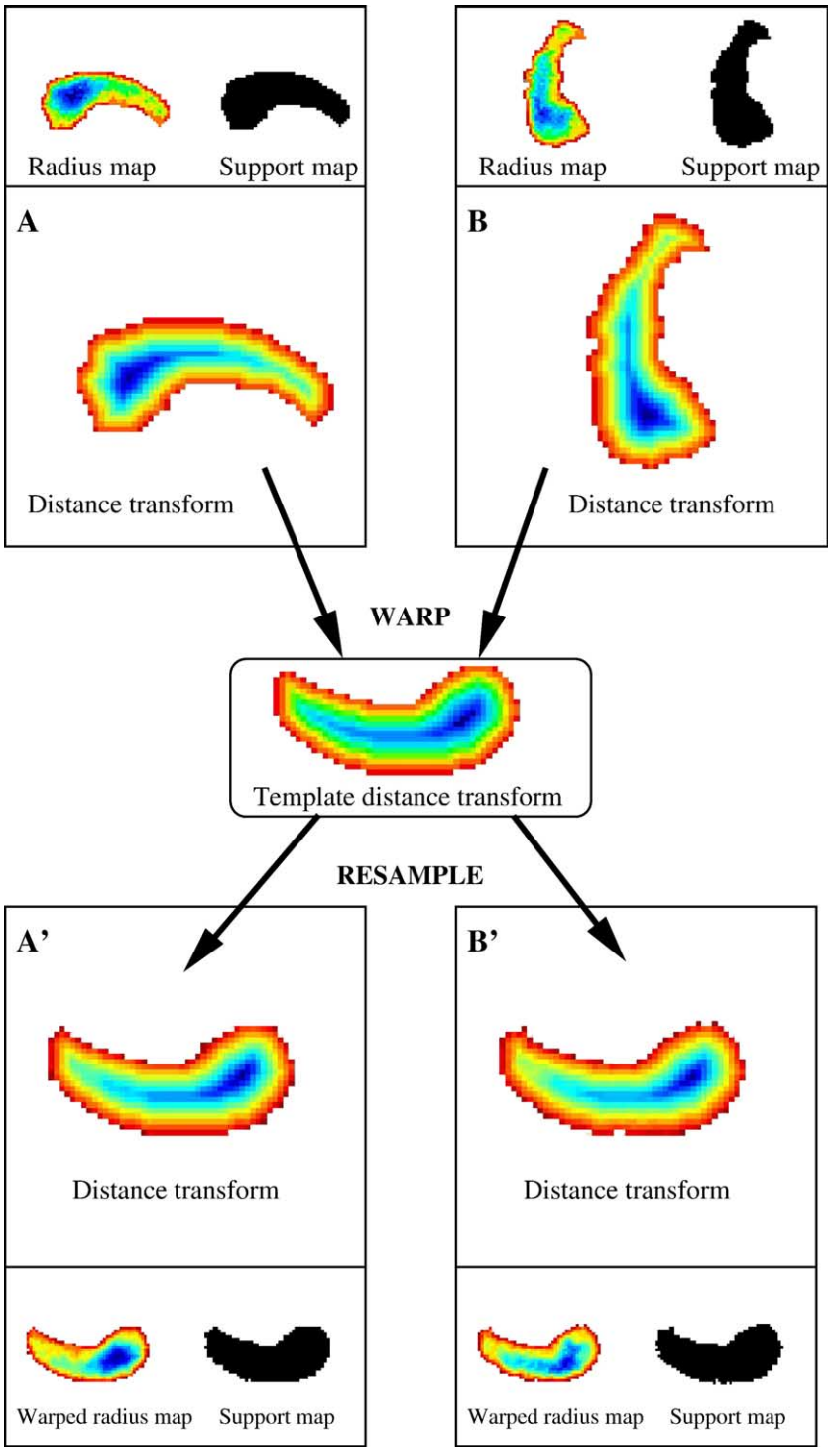

Fig. 8. Two different rigid radius maps A and B are warped to a template using their respective Euclidean distance transforms (Borgefors, 1984). The resulting distance transforms A' and B' are nearly identical to the template, thus allowing for an accurate resampling of the radius and support maps.

algorithm (Guimond et al., 2001; Thirion, 1998) to deform each flattened manifold onto a template. Since shape differences between the individual manifolds are now removed, the results of any statistical analysis have to be interpreted with some care.

Flattening

Surface flattening or more generally surface mapping is important for many applications in computer graphics, computer vision, and medical imaging. Elaborate methods have been recently developed whose goal is to map complicated surfaces such as those obtained from the cortex or the colon onto simple ones (typically spheres, cylinders, or planes) while preserving geometric properties of the object such as distance between points, area, angles, or edge orderings (Angenent et al., 1999; Drury et al., 1996; Fischl et al., 1999; Haker et al., 2000; Hermosillo et al., 1999). These methods are designed for objects with specific topologies and are often computationally expensive, e.g., they are implemented using level set methods (Hermosillo et al., 1999) or finite element methods (Angenent et al., 1999; Haker et al., 2000). This is a major drawback for the analysis of HC data over a population of individuals. An alternate framework which is both quite general as well as computationally efficient is that of multidimensional scaling (MDS) (Grossman et al., 2002; Roweis and Saul, 2000; Tenenbaum et al., 2000). Given a set of points in lD, classical MDS finds analytically the optimal layout of points in $m-$ D ($l > m$) such that the distance between any two points is approximately preserved. These methods are fast and accurate, but can lead to serious artifacts for surfaces which are non-convex such as the medial manifolds of HC data, which have "neck"-like regions (see Fig. 3c).

Thus, we employ a different flattening method, which is inspired by early work on the map making problem (Sammon, 1969; Schwartz et al., 1989). Let there be N points in $l-$ D that are to be flattened so that they lie in $m-$ D, with $l > m$. Let d^*_{ij} be the geodesic distance between points $x_i = (x_{i1}, x_{i2}, \ldots, x_{il})$ and x_j in $l-$ D and d_{ij} be the geodesic distance between the corresponding points $y_i = (y_{i1}, y_{i2}, \ldots, y_{im})$ and y_j in $m-$ D. Sammon (1969) defines an error function E based on d^*_{ij} and d_{ij}, which represents how well the m-space configuration fits the points in l-space:

$$E = \frac{1}{c} \sum_{i=1}^{N} \sum_{j=1}^{N} \left[\frac{\left(d^*_{ij} - d_{ij}\right)^2}{d^*_{ij}} \right], \tag{4}$$

where $c = \sum_{i=1}^{N} \sum_{j=i}^{N} [d^*_{ij}]$. One is essentially left with the task of moving the points y_i in order to minimize E, which can be solved using a standard gradient descent strategy. Although such a technique is not guaranteed to find the global minimum of this energy, our experiments show that this method leads to flattened medial manifolds with low distortion (Fig. 4).

Fig. 5 shows statistics of the inter-distance errors introduced by this flattening algorithm for all pairs of points over all 160 medial manifolds associated with the 80 HC volumes in the current study. In other words, there are 160 data points shown for the mean, median, and standard deviation. The errors are in fact very small, with a maximum mean error of approximately 0.45 mm. Fig. 6 shows how these errors are distributed for a single medial manifold. Here it appears that the maximum error due to flattening occurs on the medial side of the HC, near its head and its tail.

Alignment

Once the extended medial manifolds have been flattened, they can be registered using two methods. The first is a rigid body transformation which preserves the shape of each manifold but does not provide a one-to-one correspondence between them. The second is a non-rigid transformation which deforms each manifold to a template. This latter technique establishes one-to-one correspondences between the manifolds at the cost of deforming their shapes. It is important to note that the original HC label volumes were derived from stereotaxically transformed data and hence have been subjected to an initial spatial normalization based on overall brain size, position, and orientation. The rigid transformation described below is akin to a local linear transformation, further improving HC alignment without changing HC size.

Rigid alignment. The simplest technique exploits the fact that the HC volumes, and hence their associated flattened medial manifolds, have a "banana"-like shape with a clear direction along which each structure is elongated. For each flattened manifold, the centroid of all points is associated with the origin and the principal component directions with the x and y axes of a common coordinate frame. In what follows, we shall refer to medial manifolds aligned in this fashion along with their associated medial surface radius values as *rigid radius maps*. Examples of this type of alignment are illustrated in Fig. 7.

Non-rigid alignment. The second technique relies on a template created by averaging all the rigidly aligned flattened medial manifolds and thresholding this average map at the 50% level. Unfortunately, binary maps do not contain enough information to be accurately warped to each other. In order to exploit 2D shape information, we compute the Euclidean distance function (Borgefors, 1984) to the boundary of each binary map and then compute the transformation for warping each to the Euclidean distance transform of the template. Once this non-linear transformation has been computed, it can then be used to warp and interpolate the rigid radius maps. The actual warping technique is a variation of the Demons algorithm (Thirion, 1998), implemented by Guimond

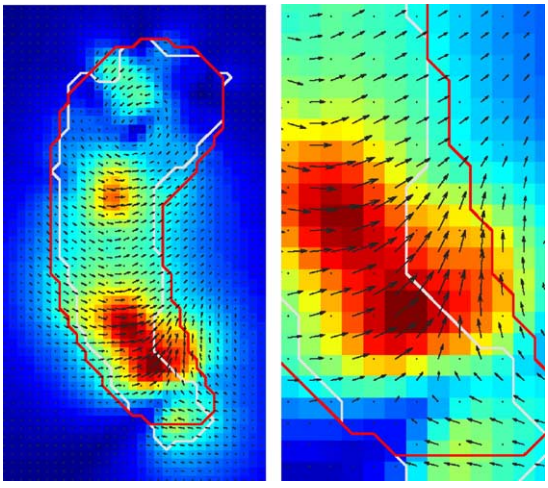

Fig. 9. A representative warping field provided by the Demons algorithm (Guimond et al., 2001; Thirion, 1998) along with a magnified view of the bottom right portion. The white outline represents the boundary of the test surface and the red outline the boundary of the target surface. The color coding shows increasing displacement from blue to red. The black vectors indicate the direction of that displacement.

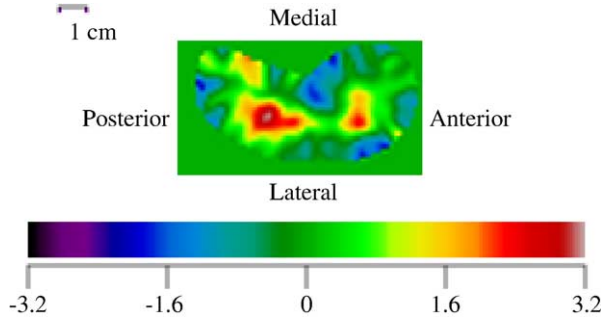

Fig. 10. An example regression map for the statistical analysis with an associated scale bar and a color bar to indicate t values. Black and white regions reach statistical significance, negatively and positively, respectively.

et al. (2001), which is well established in the medical image analysis community. The procedure is illustrated in Fig. 8. Observe that the resulting warped distance transforms (A',B') are nearly identical to the template distance transform, illustrating the robustness of the warping procedure. A representative example of a warping field obtained by this algorithm is provided in Fig. 9. In what follows, we shall refer to these flattened medial manifolds along with their associated medial surface radius values as *warped radius maps*.

Statistical analysis

Once the flattened medial manifolds had been aligned, the associated individual 2D radius maps could be averaged as well as employed for further statistical analysis, keeping in mind that the intensity information contained in each map at each point referred to the local width of the original HC. Pixel-based regression was used to localize statistically significant shape differences that are correlated with age or gender. As an example, the flattened medial surfaces were used in a linear regression model with gender as a dependent variable, age as a covariate, and the individual points on the 2D maps as dependent variables in order to compute the slope of the effect of gender on the shape of the HC. This regression was estimated at each pixel location in the 2D map. In order to detect regions that were significantly different (i.e., where the differences were above chance), it was necessary to correct for multiple comparisons and local spatial correlations. We used the random field theory of Worsley et al. (1998) to determine the t-value threshold that indicates statistically significant differences, given a selected level of α-error.

Before interpreting the regression maps, it is important to consider the type of alignment technique used to register the individual maps since the technique will affect the point-to-point homology. In most cases, a significant change in the radius function means either compression (radius decreases) or expansion (radius increases) of the corresponding surface points on the HC. This is always true in the warped maps. However, in the rigid maps, a one-to-one correspondence is not established. Thus, when there is a loss of radius along the border and a gain right next to it, it is likely to be due to a shift or bend of the flattened maps at that location. Although further analyses should be performed to confirm the shift/bend effect, the positive/negative regression pattern and a complete loss of significance in the corresponding warped maps are strong indicators of this type of shape change.

To examine the effects of both age and gender on HC shape, linear regression analyses were performed separately for each pixel, on both the rigid radius maps and the warped radius maps associated with the HC of the left and right hemispheres for all data sets. Before computing the regressions, the radius maps were blurred with a 3-mm full-width half-maximum 2D Gaussian kernel. Given the number of subjects, data resolution, pixel size, and area of search region, the critical t value for a 2-tailed α significance level of $P < 0.05$ after correcting for multiple comparisons is $|t| > 4.11$ for peak voxels and $|t| > 3.2$ for clusters of more than 4.5 voxels, according to the random field theory of Worsley et al. (1998). Fig. 10 is an example regression map where the anterior, posterior, lateral, and medial regions of the HC are identified, and where a scale bar as well as a color bar indicating t values are shown. The data are presented in a spectral color scale, from -3.2 to 3.2. Black and white regions reach statistical significance, negatively and positively, respectively. Almost significant negative regions are purple and almost significant positive regions are red.

Validation of method

Registration and alignment

Fig. 11 shows the results of the rigid and non-rigid registration of the radius maps for all subjects. The support maps of the rigid

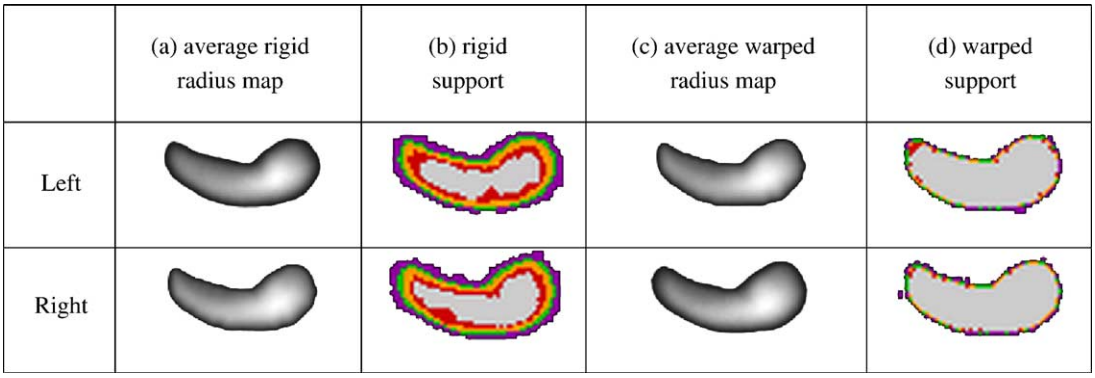

Fig. 11. This figure illustrates levels of support associated with the medial manifolds of the left and right HC datasets. In the second and fourth columns, gray regions indicate locations covered by 100% of the flattened medial manifolds. Coverages by 90%, 70%, 50%, 30%, and 10% of the entire HC data set are obtained by adding the red, orange, green, indigo, and black regions, respectively.

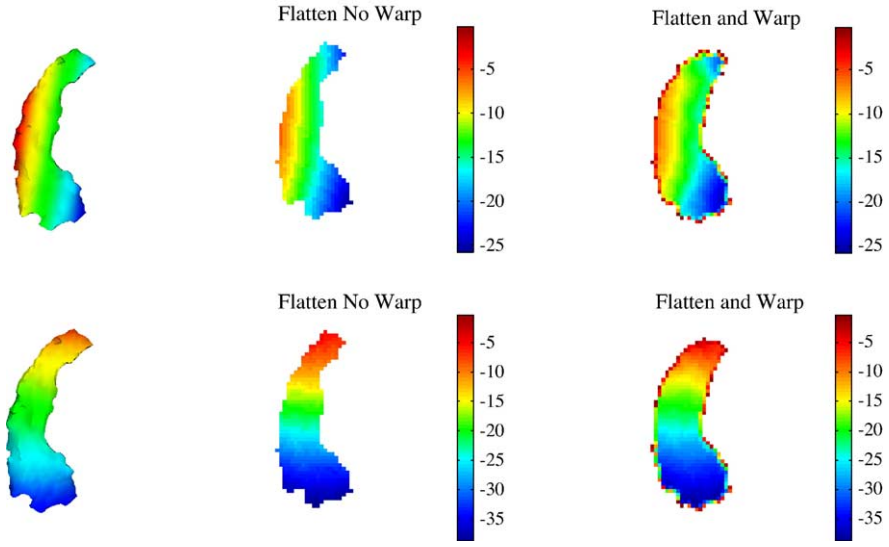

Fig. 12. Gradations of intensity are created on an original 3D medial manifold (left column) and then mapped to the plane using the flattening process (middle column) followed by warping to the average template (right column). Results are shown for a lateral to medial gradation (top row) and a posterior to anterior gradation (bottom row). In both cases, the gradation is stretched but is otherwise preserved.

radius maps shown in column b demonstrate that there is a significant overlap across all subjects in the middle of the map, although the overlap decreases significantly towards the edge. This decrease is explained by anatomical differences of HC shape between subjects, which is not corrected for by rigid registration. After a registration based on warping (column d), the fit is much better toward the edges, indicating a high degree of alignment for the warped support maps between all subjects. This non-rigid registration also results in an improved point-to-point homology between the associated radius maps.

In order to qualitatively demonstrate that the flattening and warping steps preserve local spatial relationships we created two different gradations of intensity on the original medial manifolds and examined them after each of these steps were applied. The results are presented in Fig. 12 for a lateral to medial gradation (top row) and a posterior to anterior gradation (bottom row). Both of these indicate that the gradation, though stretched, is preserved. This suggests that the mapping of 3D medial manifold points to points on the 2D average template is smooth.

Simulated shape changes

We carried out a quantitative validation by evaluating the method using simulated (known) shape changes. We selected the

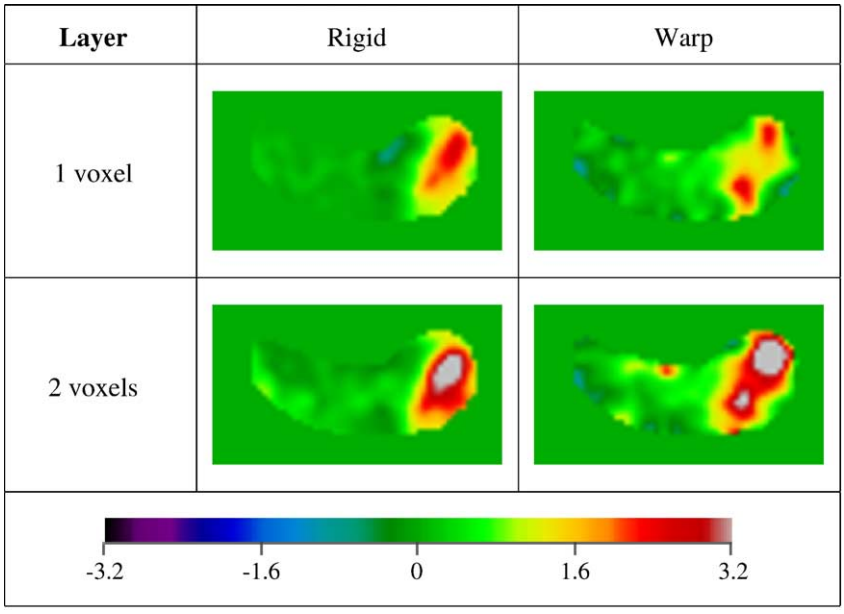

Fig. 13. A linear regression was carried out comparing radius maps for the left HC volumes of 33 female subjects with those obtained for the same volumes, but with a layer of voxels added to the top of the head of the HC.

Table 1
Volume statistics for the HC volumes used in the validation experiment

Group	n	Mean volume	Standard deviation of volume
Original	33	4110	398
1 mm	33	4281	408
2 mm	33	4426	421

left HC volumes of 33 female subjects and created a second data set by adding a layer of voxels to the top of the head of the HC for each volume. We then ran linear regressions to compare the radius maps associated with each data set. For this experiment, the critical t value for a 2-tailed α significance level of $P < 0.05$ after correcting for multiple comparisons is $|t| > 4.59$ for peak voxels and $|t| > 3.21$ for clusters of more than 7 voxels, according to the random field theory of Worsley et al. (1998). The results are shown in Fig. 13. With a 1-voxel layer addition, the results show a trend toward significance, but neither the peak values nor the clusters reach significance. With a 2-voxel layer addition, significant localized differences can be observed both before and after warping and these differences are properly located at the head of the HC.

Statistics based only on the volume of the different HC data sets correlate well with the above results. A two-tailed t test comparing original HCs vs. HCs with an additional layer gives $P = 0.08567$ for the 1 voxel case, which is not significant, but $P = 0.002281$ for the 2-voxel case, which is highly significant (Table 1).

Results

When examining the results from the regression for gender differences after controlling for the effects of age (Fig. 14), a portion in the body of the HC on the lateral side approaches significance ($t = 3.1$) in the left hemisphere in the rigid radius maps. This difference almost disappears in the warped map. There could be an expansion of the corresponding surface points of the HC; however, one should be cautious with this claim considering that this positive region is located near the medial manifold border. In the right hemisphere, in the rigid radius maps, there are both positive and negative regression effects in the posterior medial portion of the HC tail approaching significance ($t = 3.1$ and $t = -3.1$). The positive medial region at the tail of the hippocampus is balanced by an almost equivalent negative region on the lateral side. This effect, combined with its disappearance in the warped map, suggests that the difference is due to a shifting or bending of the HC and hence the rigid maps, as discussed in Statistical analysis.

Fig. 15 illustrates the effects of age on the radius maps for both left and right hemispheres for women. Within women, a positive regression with age can be found along a strip in the medial portion in the anterior HC, corresponding to the area of the gyrus intralimbicus, in the left hemisphere, approaching significance ($t = 3.1$). In the right hemisphere, there is a very small portion in the transition from body to head of the HC, in the midline of the structure, which approaches significance for a negative regression value ($t = -3.1$). In the warped maps, these tendencies either disappear (right hemisphere) or are significantly reduced in size (left hemisphere), indicating that there are probably no significant changes with respect to age in women.

Within the group of men, a different picture emerges as shown in Fig. 16. Here, the results show a consistent pattern of negative regression with age in both the left and right hemispheres in the rigid radius maps, which can be observed towards the lateral border of the HC head, and towards the midline of the tail ($t < -3.2$, size > 7 voxels). In addition, in the right hemisphere, there is an area in the medial portion of the HC head that reaches significance ($t < -3.2$, size > 7 voxels). In the warped maps, there is a small portion in the anterior medial part of the HC, corresponding to the HC head, where effects reach significance in the left hemisphere ($t < -3.2$, size > 7 voxels), and approach significance in the right hemisphere ($t < -3.1$, size > 7 voxels). These results suggest strongly that there is a compression of the surface of the HC in the lateral and medial part of the head. As was

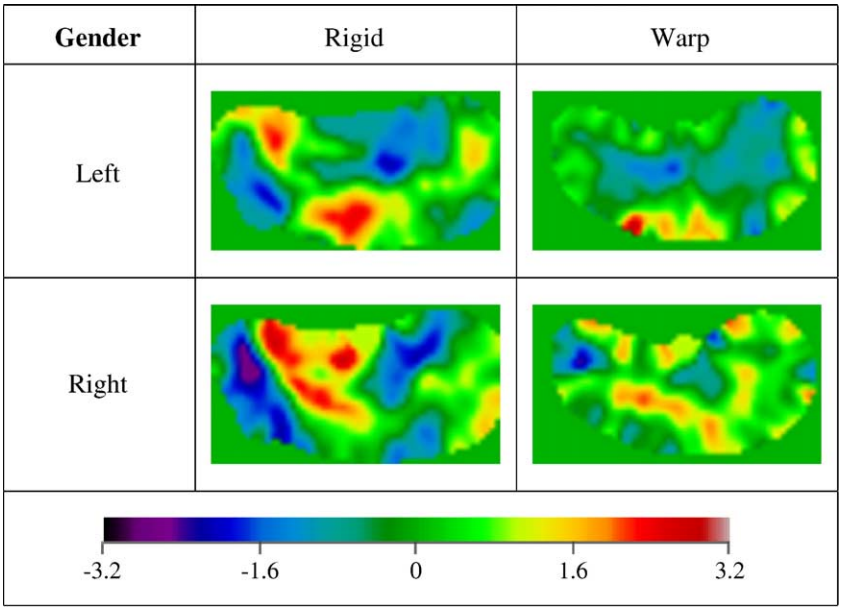

Fig. 14. Linear regressions to examine the effects of gender, having corrected for age, on the radius maps.

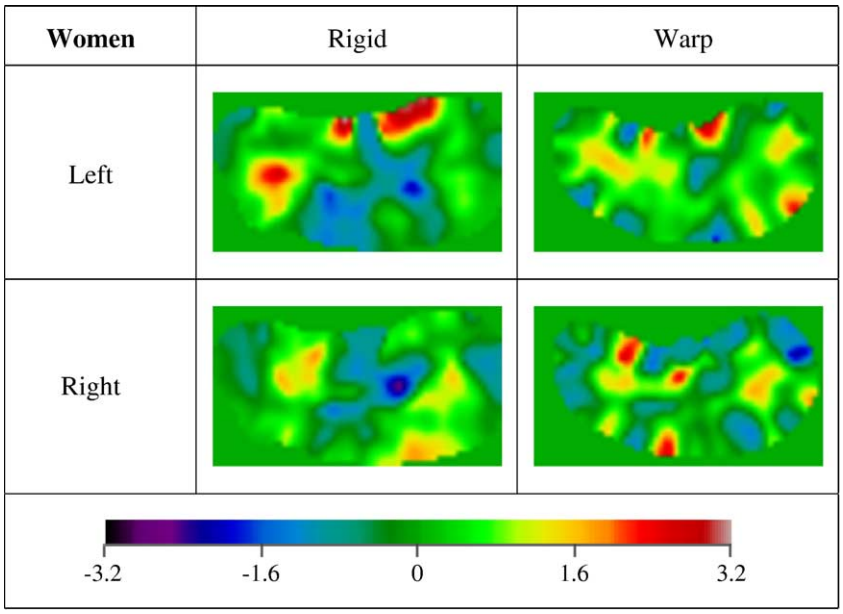

Fig. 15. Linear regressions to examine the effects of age on the radius maps for women.

the case for the analysis of all the data (Fig. 14), there are negative and positive regions near the tail of the hippocampus in the rigid map that disappear in the warped map, which is likely to be explained by a shifting or bending of the HC.

Discussion

Using quantified HC volumes from a recently developed segmentation protocol (Pruessner et al., 2000), a gender-specific age-related volume decline was observed in a healthy population of men and women in early adulthood in a previous study (Pruessner et al., 2001). This earlier study investigated signal-intensity changes within the HC volumes using voxel-based regressions and showed that within the group of women a signal-intensity increase was apparent mostly in the middle portion of the HC along the superior border, where white-matter structures lie adjacent to the HC (alveus and fimbria). In contrast, in the group of men, a signal-intensity decrease was observed in areas adjacent to ventricular space (lateral rim: inferior horn of the lateral ventricle; medial rim: quadrogeminal cistern and uncal recess of the inferior horn of the lateral ventricle). This led to the conclusion that the observed HC volume decline with age in the group of men was caused by a decline of HC volume with an accompanying volume increase of the adjacent ventricles (Pruessner et al., 2001). However, due to variability in HC shape and positioning in

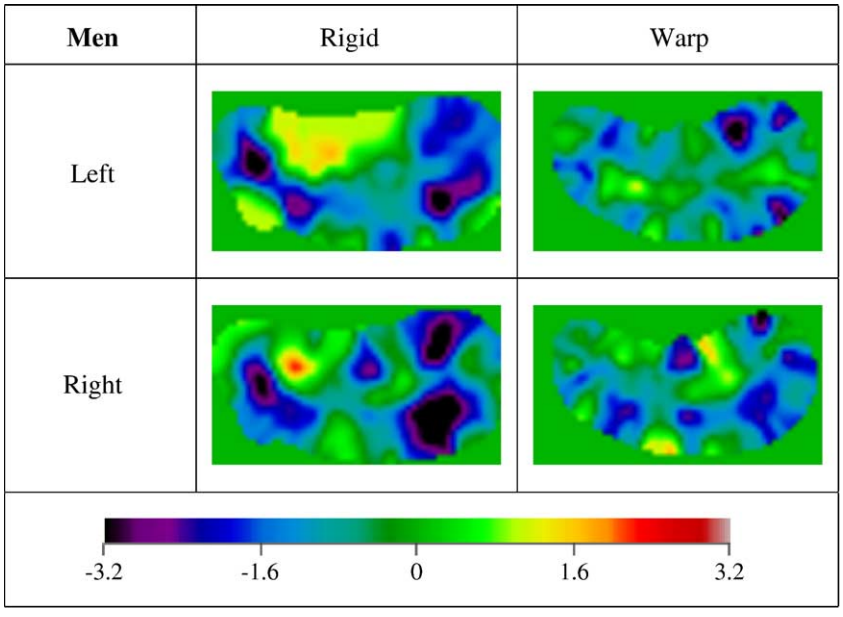

Fig. 16. Linear regressions to examine the effects of age on the radius maps for men.

three-dimensional space, the precise location of these volume changes could not be determined. The current study, where HC shape is analyzed using medial surfaces, is able to complement and extend the previously observed findings.

In the experiment simulating shape changes, the HC labels from each member of a group of 33 female subjects were modified by adding one and two layers of voxels, respectively, to the top of the anterior 10 mm of the HC volumes. The two groups of modified labels were then compared to the original unmodified labels using the shape-analysis procedure (medial surface extraction, flattening, and rigid or warped alignment). The results of the regression, clearly indicating significant differences in the expected location for the two layer voxel group, and showing a trend for the one layer voxel group, demonstrate the sensitivity and the spatial specificity of the procedure. The amount of change that was introduced by the process of adding voxels, approximately 4% for the one layer voxel group and 7% for the two layer voxel group, indicates that the procedure is as sensitive in the detection of changes as are manual segmentation protocols of the HC. The latter usually have an inter-rater reliability that is around 5% (Pruessner et al., 2000; Watson et al., 1992). However, in contrast to manual segmentation protocols, the current procedure allows for a determination of the location of changes within the structure, giving it a clear advantage over competing methods.

It can be difficult to judge with certainty which anatomical correlates are associated with each observed effect in the radius maps. However, when rigid maps and warped maps agree on a loss (or gain) of radius, one can safely conclude that the radius maps reflect a compression (or expansion) of the corresponding surface points of the HC. In this study, a compression of the HC head in males with respect to age was observed. This is an important addition to previously available tools which are often unable to locate such effects with certainty. For example, in voxel-based morphometry, the results are based on differences in the gray matter density maps which can be caused by a number of factors. This has been noted in the literature and the suggestion has been made to ensure proper registration of all images prior to VBM analysis (Bookstein, 2001). However, since the goodness of fit of the registration is not normally investigated quantitatively, such studies are not immune to the impact of imperfect registration. Combined with manual segmentation protocols, the current method makes it possible to determine the location of compression/expansion of the structure of interest. Furthermore, since the technique is fully automatic and allows for the analysis of within-structure differences, it is superior with respect to reliability to techniques based on the manual labeling of complete structures.

One potential caveat of using this method is that it might present a more conservative approach compared to other volumetric analysis techniques. The radius maps are likely to explain not all the existing volumetric variability, and variability due to differences in medial manifold shape is lost after the warping.

In its current form, we suggest that our method of radius map analysis of MRI structures based on aligning flattened medial manifolds be used in conjunction with already established quantification methods. In cases such as voxel-based morphometry, the addition of a radius map-based analysis might allow for a better evaluation of the results with respect to underlying volume differences. Furthermore, due to the correspondence between medial manifold points and points on the original HC surfaces, in future studies available anatomical labels on the surface could be incorporated into the analysis, and geometric quantities other than radius (e.g., principal curvatures on the surface) could be considered. Since no data are currently available comparing MRI radius map analysis of the HC with other approaches, such studies will have to demonstrate the effectiveness of our framework. We believe that in combination with manual or automatic volume quantification methods, potentially important additional information can be derived.

Acknowledgments

We acknowledge the support of NIH, NAC, the Department of Veterans Affairs, the Natural Sciences and Engineering Research Council of Canada, the Fonds de recherche sur la nature et les technologies (FQRNT, Québec), and the Fonds de la recherche en santé (FRSQ, Québec).

References

Angenent, S., Haker, S., Tannenbaum, A., Kikinis, R., 1999. On the Laplace Beltrami operator and brain surface flattening. IEEE Trans. Med. Imaging 18, 700–711.

Attali, D., di Baja, G.S., Thiel, E., 1997. Skeleton simplification through non-significant branch removal. Image Process. Commun., 63–72.

Blum, H., 1973. Biological shape and visual science. J. Theor. Biol. 38, 205–287.

Bookstein, F.L., 1997. Shape and the information in medical images. Comput. Vision Image Underst. 66 (2), 97–118.

Bookstein, F.L., 2001. Comments: "voxel-based morphometry" should not be used with imperfectly registered images. NeuroImage 14 (6), 1454–1462.

Borgefors, G., 1984. Distance transformations in arbitrary dimensions. CVGIP 27, 321–345.

Bouix, S., Pruessner, J.C., Collins, D.L., Siddiqi, K., 2001. Hippocampal shape analysis using medial surfaces. MICCAI, Lect. Notes Comput. Sci. vol. 2208. Springer, Utrecht, The Netherlands, pp. 33–40 (October).

Brechbuhler, C., Gerig, G., Kubler, O., 1995. Parameterization of closed surfaces for 3D shape description. CVGIP, Image Underst. 61, 154–170.

Collins, D.L., Neelin, P., Peters, T.M., Evans, A.C., 1994. Automatic 3D inter-subject registration of MR volumetric data in standardized Talairach space. J. Comput. Assist. Tomogr. 18, 192–205.

Cootes, T., Taylor, C.J., Cooper, D.H., 1995. Active shape models—their training and applications. Comput. Vision Image Underst. 61, 38–59.

Corkin, S., Amaral, D.G., Gonzalez, R.G., Johnson, K.A., Hyman, B.T., 1997. H.M.'s medial temporal lobe lesion: findings from magnetic resonance imaging. J. Neurosci. 17 (10), 3964–3979.

Csernansky, J.G., Joshi, S., Wang, L., Haller, J.W., Gado, M., Miller, J.P., Grenander, U., Miller, M.I., 1998. Hippocampal morphometry in schizophrenia by high dimensional brain mapping. Proc. Natl. Acad. Sci. 95 (19), 11406–11411.

Damon, J., 2003. Determining the geometry of boundaries of objects from medial data (preprint).

Dimitrov, P., Damon, J.N., Siddiqi, K., 2003. Flux invariants for shape. CVPR'2003. Madision, Wisconsin, pp. 835–841 (June).

Drury, H.A., Van Essen, D.C., Anderson, C.H., Lee, C.W., Coogan, T.A., Lewis, J.W., 1996. Computerized mappings of the cerebral cortex: a multiresolution flattening method and a surface-based coordinate system. J. Cogn. Neurosci. 8 (1), 1–28.

Fischl, B., Sereno, M.I., Dale, A.M., 1999. Cortical surface-based analysis II: inflation, flattening, and a surface-based coordinate system. NeuroImage 9, 195–207.

Giblin, P., Kimia, B., 2004. A formal classification of 3D medial axis points and their local geometry. IEEE Trans. Pattern Anal. Mach. Intell. 26 (2), 238–251.

Golland, P., Grimson, W.E.L., Kikinis, R., 1999. Statistical shape analysis using fixed topology skeletons: corpus callosum study. IPMI'1999. LNCS, pp. 382–387.

Grossman, R., Kiryati, N., Kimmel, R., 2002. Computational surface flattening: a voxel-based approach. IEEE Trans. Pattern Anal. Mach. Intell. 24 (4), 433–441 (April).

Guimond, A., Roche, A., Ayache, N., Meunier, J., 2001. Three-dimensional multimodal brain warping using the demons algorithm and adaptive intensity corrections. IEEE Trans. Med. Imaging 20 (1), 58–69 (January).

Haker, S., Angenent, S., Tannenbaum, A., Kikinis, R., 2000. Nondistorting flattening maps and the 3D visualization of colon CT images. IEEE Trans. Med. Imaging 19, 665–670.

Hermosillo, G., Faugeras, O., Gomes, J., 1999. Cortex unfolding using level set methods. Proceedings of the Second International Conference on Scale-Space Theories in Computer Vision, LNCS, vol. 1682. Springer-Verlag, London, UK, pp. 58–69. September, Corfu, Greece.

Joshi, S., Pizer, S.M., Fletcher, P.T., Thall, A., Tracton, G., 2001. Multiscale 3D deformable model segmentation based on the medial description. IPMI'2001, pp. 64–77.

Malandain, G., Bertrand, G., Ayache, N., 1993. Topological segmentation of discrete surfaces. Int. J. Comput. Vision 10 (2), 183–197.

Mangin, J.F., Poupon, F., Riviere, D., Cachia, A., Evans, A.C., Collins, D.L., Regis, J., 2003. 3D moment invariant based morphometry. In: Ellis, R.E., Peters, T.M. (Eds.), MICCAI, LNCS, vol. II, pp. 505–512.

Mori, E., Yoneda, Y., Yamashita, H., Hirono, N., Ikeda, M., Yamadori, A., 1997. Medial temporal structures relate to memory impairment in Alzheimer's disease: an MRI volumetric study. J. Neurol., Neurosurg. Psychiatry 63 (2), 214–221.

Näf, M., Kübler, O., Kikinis, R., Shenton, M.E., Sźekely, G., 1996. Characterization and recognition of 3D organ shape in medical image analysis using skeletonization. IEEE Workshop on Mathematical Methods in Biomedical Image Analysis, pp. 139–150.

Pizer, S.M., Fritsch, D.S., Yuskhevich, P., Johnson, V., Chaney, E., 1999. Segmentation, registration and measurement of shape variation via image object shape. IEEE Trans. Med. Imaging 18, 851–865.

Pizer, S.M., Chen, J.Z., Fletcher, P.T., Fridman, Y., Fritsch, D.S., Gash, A.G., Glotzer, J.M., Jiroutek, M.R., Joshi, S., Lu, C., Muller, K.E., Thall, A., Tracton, G., Yushkevich, P., Chaney, E.L., 2003. Deformable M-reps for 3D medical image segmentation. Int. J. Comput. Vision 55 (2), 85–106.

Pruessner, J.C., Li, L.M., Serles, W., Pruessner, M., Collins, D.L., Kabani, N., Evans, A.C., 2000. Volumetry of hippocampus and amygdala with high-resolution MRI and 3D analyzing software: minimizing the discrepancies between laboratories. Cereb. Cortex 10, 433–442.

Pruessner, J.C., Collins, D.L., Pruessner, M., Evans, A.C., 2001. Age and gender predict volume decline in the anterior and posterior hippocampus in early adulthood. J. Neurosci. 21 (1), 194–200.

Pudney, C., 1998. Distance-ordered homotopic thinning: a skeletonization algorithm for 3D digital images. Comput. Vision Image Underst. 72 (3), 404–413.

Roweis, S.T., Saul, L.K., 2000. Nonlinear dimensionality reduction by locally linear embedding. Science 290, 2323–2326 (December).

Sammon, J.W., 1969. A nonlinear mapping for data structures analysis. IEEE Trans. Comput. C 18 (5), 401–409 (May).

Schacter, D.L., Wagner, A.D., 1999. Medial temporal lobe activations in fMRI and PET studies of episodic encoding and retrieval. Hippocampus 7 (1), 7–24.

Schwartz, E.L., Shaw, A., Wolfson, E., 1989. A numerical solution to the generalized mapmaker's problem: flattening nonconvex polyhedral surfaces. IEEE Trans. Pattern Anal. Mach. Intell. 11 (9), 1005–1008 (September).

Siddiqi, K., Bouix, S., Tannenbaum, A., Zucker, S.W., 2002. Hamilton–Jacobi skeletons. Int. J. Comput. Vision 48 (3), 231–251.

Sled, J.G., Zijdenbos, A.P., Evans, A.C., 1998. A non-parametric method for automatic correction of intensity non-uniformity in MRI data. IEEE Trans. Med. Imaging 17 (1), 87–97.

Styner, M., Gerig, G., 2001. Medial models incorporating object variability for 3D shape analysis. IPMI'2001, pp. 502–516.

Styner, M., Gerig, G., Lieberman, J., Jones, D., Weinberger, D., 2003a. Statistical shape analysis of neuroanatomical structures based on medial models. Med. Image Anal. 7 (3), 207–220.

Styner, M., Lieberman, J., Gerig, G., 2003b. Boundary and medial shape analysis of the hippocampus in schizophrenia. In: Ellis, R.E., Peters, T.M. MICCAI, vol. 2, pp. 464–471.

Tenenbaum, J.B., de Silva, V., Langford, J.C., 2000. A global geometric framework for nonlinear dimensionality reduction. Science 290, 2319–2323 (December).

Thirion, J.P., 1998. Image matching as a diffusion process: an analogy with Maxwell's demons. Med. Image Anal. 2 (3), 243–260.

Thomson, P.M., Miller, M.I., Ratnather, T., Poldrack, R.A., Nichols, T.E., 2004. Mathematics in brain imaging. NeuroImage, vol. 23 (Suppl. 1). Elsevier.

Watson, C., Andermann, F., Gloor, P., Jones-Gotman, M., Peters, T., Evans, A., Olivier, A., Melanson, D., Leroux, G., 1992. Anatomic basis of amygdaloid and hippocampal volume measurement by magnetic resonance imaging. Neurology 42 (9), 1743–1750.

Worsley, K.J., Poline, J.B., Evans, A.C., 1998. Characterizing the response of PET and fMRI data using multivariate linear models. NeuroImage 6, 305–319.